ELSEVIER

Contents lists available at ScienceDirect

## Computer Methods and Programs in Biomedicine

journal homepage: www.sciencedirect.com/journal/computer-methodsand-programs-in-biomedicine





## Fluid-structure interaction study of penetrating atherosclerotic ulcers: Assessing progression and rupture risks

Tian Wu<sup>a</sup>, Hong Zhu<sup>a</sup>, Haoyu Zhuo<sup>a</sup>, Jiang Li<sup>b,\*</sup>, Jie Xiao<sup>a,\*</sup>

- <sup>a</sup> School of Chemical and Environmental Engineering, College of Chemistry, Chemical Engineering and Materials Science, Soochow University, Suzhou, Jiangsu, 215123, China
- b Department of Vascular Surgery, Affiliated Suzhou Hospital of Nanjing Medical University, Suzhou, Jiangsu, 215000, China

#### ARTICLE INFO

#### Keywords:

Penetrating atherosclerotic ulcer (PAU) Computational hemodynamics Fluid-structure interaction Time-averaged wall shear stress Von Mises stress

#### ABSTRACT

Background and objective: Penetrating atherosclerotic ulcer (PAU) is a distinct pathology in acute aortic syndrome that may progress to aortic dissection or rupture. Conservative management, which primarily focuses on controlling blood pressure and heart rate, is prone to failure. The construction of numerical simulation models to predict and analyze the PAU progression and rupture risks will aid clinicians in understanding and improving PAU management and treatment.

*Methods*: In this study, fluid-structure interaction simulations were employed to investigate the biomechanical characteristics of PAUs under various conditions, aiming to assess their risks of rupture and progression. Further correlation analyses were conducted to identify dominant factors influencing ulcer progression. A quantitative comparison of progression risk was conducted between a single big PAU and two small PAUs with equivalent total volumes.

Results: The results demonstrate that as the PAU radius increases to 10 mm, the time-averaged wall shear stress (TAWSS) in the PAU dome region gradually decreases, falling significantly below the physiological range (1.0–3.0 Pa). Elevated blood pressure and heart rate primarily promote PAU rupture by influencing von Mises stress and displacement. Additionally, correlation analyses demonstrate that neither reducing blood pressure nor heart rate is sufficient to restore TAWSS to the physiological range (1.0–3.0 Pa). A single big PAU exhibits lower TAWSS in the dome region, indicating a higher progression risk compared to two small PAUs.

Conclusion: The evidence quantitatively supports the limitations of conservative management in halting PAU progression. Notably, a single big PAU carries a higher progression risk compared to two small PAUs, necessitating increased clinical intervention and monitoring.

#### 1. Introduction

Penetrating atherosclerotic ulcer (PAU) is a distinct pathology in acute aortic syndrome that includes aortic dissection, intramural hematoma, and more. PAU is characterized by an ulcerated atherosclerotic plaque that penetrates through the intima and elastic lamina layers of the aortic wall, extending into the media [1]. If left untreated, PAU may progress to severe complications such as aortic pseudoaneurysm, aortic dissection, or other acute aortic syndromes [2]. Diagnosing PAU based solely on clinical presentation is challenging, as it often remains asymptomatic [3]. Notably, a report [4] has documented a rupture rate of 40 % in PAU with a malignant course, which is higher than that observed in other acute aortic syndromes. The spatial distribution of

PAU lesions varies widely along the aorta, with a predominant occurrence in the descending aorta [5]. Due to the relatively low incidence of PAU, there is a lack of dedicated randomized controlled trials (RCTs) to guide management [4]. However, extensive clinical analyses have led to the development of several decision-making frameworks for PAU treatment. Conservative therapy, including radiological surveillance and antihypertensive therapy, is generally recommended for PAUs located in the descending aorta, while thoracic endovascular aortic repair (TEVAR) is preferred for acute cases. Emergency surgery is normally the preferred treatment option for acute PAUs in the ascending aorta or aortic arch [6]. In addition, some reports [2] suggest that conservative therapy is advisable for small asymptomatic PAUs with a diameter of <20 mm or a depth of <10 mm, as these PAUs are associated

E-mail addresses: doctormaxli@protonmail.com (J. Li), jie.xiao@suda.edu.cn (J. Xiao).

<sup>\*</sup> Corresponding authors.

with lower risks of progression and rupture. It has also been reported that PAU patients with hypertension, diabetes, and hyperlipidemia should have more frequent surveillance [2]. Recent reports suggest that conservative management of PAUs is less effective compared with endovascular treatment [5,7].

However, the underlying mechanisms of PAU progression and rupture are complicated and remain unclear, and the appropriate treatment strategies are not well-explained, relying heavily on clinical experience. To address these gaps, scholars have made numerous efforts. It is now widely recognized that the geometric characteristics of a lesion determine the biomechanical factors within the affected tissue and abnormalities in these factors can lead to the development of aortic disease [8]. The primary biomechanical factors that have been investigated so far involve wall shear stress (WSS) and tissue stress (von Mises stress). WSS is the tangential stress due to the friction of the flowing blood on the endothelial surface of the vascular wall. Endothelial cells in the vascular wall detect various shear stress signals through mechanical receptors. Then these receptors convert mechanical signals into cellular responses, resulting in changes to the structure and function of the vessel wall [9,10]. Physiological WSS (1.0-3.0 Pa) is essential for maintaining the normal phenotype of the vascular wall [11]. However, both low WSS (<1.0 Pa) and high WSS (>3.0 Pa) can promote the progression of vascular lesions through multiple mechanisms. These mechanisms include endothelial cell dysfunction, triggering of inflammatory responses, accumulation and oxidation of low-density lipoprotein (LDL), proliferation and migration of smooth muscle cells (SMCs), abnormal platelet activation, and disruption of the endothelial glycocalyx [12]. Tissue stress (von Mises stress) serves as a critical indicator of the stress condition within the vessel wall. It quantifies the internal structural stress experienced by the vessel wall due to the action of blood pressure. When this stress value becomes excessively high, surpassing the yield stress threshold of the vessel wall material, the vessel wall is at risk of rupture [13].

Currently, the application of computational fluid dynamics (CFD) technology in the clinic enables more accurate acquisition of hemodynamics at the lesion site [14,15]. Consequently, hemodynamic parameters, including WSS, are increasingly recognized as important indicators of the risk of aortic disease progression and rupture [14,16]. Fluid-structure interaction (FSI) simulates the interaction between fluid and solid domains by integrating fluid dynamics, solid mechanics, and fluid-solid interface coupling. This approach can be employed to investigate the impact of biomechanical parameters on aortic diseases. Compared to CFD, FSI not only provides the hemodynamic characteristics of the blood flow field including WSS, but also provides crucial biomechanical metrics of the vessel wall, such as tissue stress (von Mises stress) and displacement. Currently, FSI has been extensively employed in the simulation and modeling of diseases such as aortic dissection and aneurysms. Philip et al. [17] revealed that variations in the morphological characteristics of cerebral aneurysms result in distinct hemodynamic and biomechanical behaviors. Valencia et al. [18] showed that dynamic factors, such as hypertension and pressure gradients, can influence wall stress and WSS, thereby affecting the risk of aneurysm rupture. Valeti et al. [19] further demonstrated through FSI simulations that regions with thinner walls in patient-specific cerebral aneurysms are more susceptible to rupture. Additionally, a related study [13] investigated the effect of aspect ratio on aneurysm rupture risk, revealing that aneurysms with larger aspect ratios and thinner walls exhibit lower WSS and higher effective wall stress, potentially increasing rupture risk. Furthermore, studies have shown that higher time-averaged wall shear stress (TAWSS) and lower oscillatory shear index (OSI) during motion are associated with a reduced risk of atherosclerosis and thrombus formation within aneurysms [20]. In the context of aortic dissection, one study [21] reported that increased stiffness of the dissection wall is associated with a higher risk of disease progression. Another study [22] demonstrated that stress state, WSS, and flow characteristics are the primary parameters influencing the

progression of aortic dissection. Jia et al. [23] investigated the relationship between hemodynamics and the pathogenesis of superior mesenteric artery dissection. Moreover, recent studies [22,24] have incorporated the fiber-reinforcement effect of the vessel wall, employing more realistic fiber-reinforced hyperelastic vessel wall models to further explore the relationship between hemodynamics and disease progression in aortic dissection.

However, PAU, characterized by a mechanical response to the interaction between blood flow and the damaged vascular wall, exhibits a distinct progression and rupture process compared to other acute aortic syndromes (such as aortic aneurysm and aortic dissection), owing to its particular geometry and characteristics [25]. In a study [26] employing FSI analysis, researchers evaluated hemodynamic parameters before and after thoracic endovascular aortic repair (TEVAR). They found that the PAU region experiences blood stagnation, resulting in elevated intraluminal pressure and reduced WSS, which ultimately contribute to PAU progression. Despite these insights, the influence of biological factors—such as ulcer size, location, blood pressure, and heart rate—on PAU progression and rupture remains poorly understood. Elucidating these factors is critical, as it would enable quantitative predictions of PAU progression and rupture risks, thereby informing and optimizing clinical decision-making for PAU treatment.

The aim of this study is to quantitatively evaluate the effects of biological factors, such as ulcer size and location, as well as blood pressure and heart rate, on the progression and rupture risks of PAU using FSI analysis. Specifically, biomechanical parameters including WSS and von Mises stress in the PAU region were calculated. These parameters were subsequently employed as quantitative metrics to assess the progression and rupture risks of PAU. Furthermore, a correlation analysis was conducted to elucidate the effects of the aforementioned biological factors on the biomechanical parameters within the PAU region, thereby revealing the underlying mechanisms through which these factors influence the progression and rupture risks of PAU. Additionally, the question of whether a single big PAU or two small PAUs carries a greater risk of progression was explored, a scenario commonly encountered by clinicians.

## 2. Modelling and simulation methods

#### 2.1. Geometric configuration

A 3-dimensional idealized model of the thoracic aorta with a PAU was constructed based on a related study [27]. It has similar geometry and characteristics to the real thoracic aorta that includes the ascending aorta (AA), aortic arch and its three branches: the brachiocephalic artery (BA), left common carotid artery (LCA), and left subclavian artery (LSA), as well as the descending aorta (DA). The non-planarity of the aorta and the spatial variation in aortic diameter were considered. A schematic representation of the aortic model is provided in Fig. 1.

Based on clinical CT images, anatomical data, and schematic drawings [1,2], it has been observed that a PAU typically appears geometrically as a spheroidal cavity on the aortic wall. In the search of PAU cases, it was found that the average growth rate of PAU depth was  $\sim\!\!0.5$  mm/year, and the average growth rate of neck width was  $\sim\!\!1.1$  mm/year [4]. For our analysis, the PAU depth was approximated as the radius, and the neck width was approximated as the diameter, with the latter being twice the former. Therefore, the PAU geometry was simplified to a truncated spherical cavity, as shown in Fig. 1.

## 2.2. Governing equations

## 2.2.1. Fluid flow model

The Eulerian and Lagrangian methods are commonly utilized to simulate fluid flow and solid deformation, respectively. The equations of mass and momentum conservation for fluid flow are presented as follows:

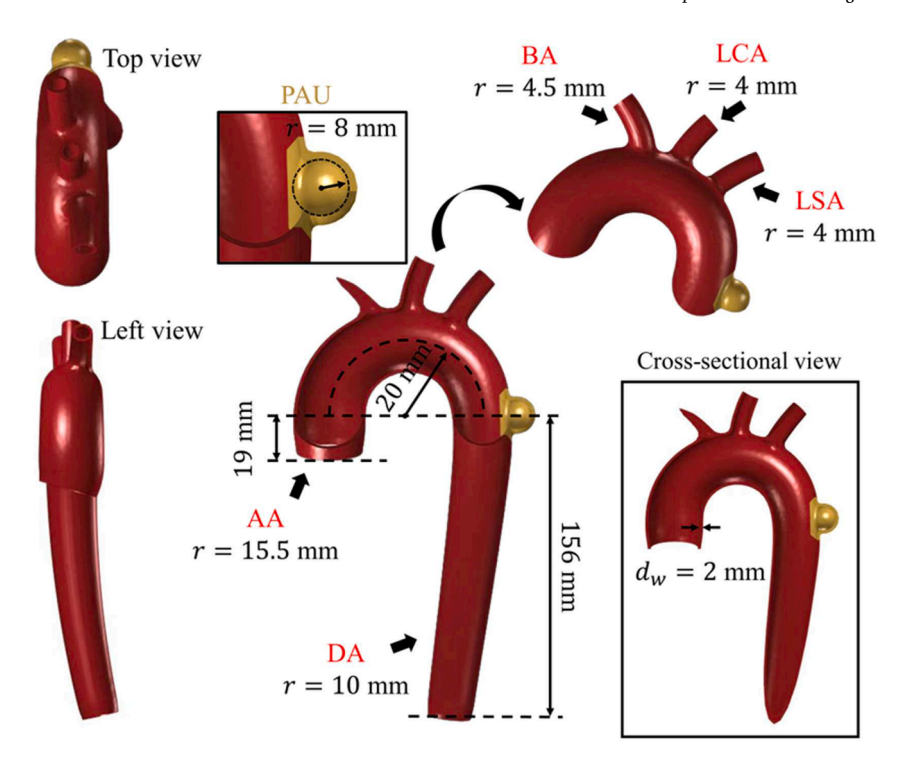


Fig. 1. Schematic diagrams of the model geometry (AA: ascending aorta; BA: brachiocephalic artery; LCA: left common carotid artery; LSA: left subclavian artery; DA: descending aorta). The red part is the vascular wall, and the yellow part is the PAU.

$$\rho_f \nabla \cdot (u_f) = 0 \tag{2.1}$$

$$\rho_{f} \frac{\partial u_{f}}{\partial t} + \rho_{f} ((u_{f} - u_{m}) \cdot \nabla) u_{f} = -\nabla p + \nabla (\mu (\nabla u_{f} + (\nabla u_{f})^{T})$$
(2.2)

where  $\rho_f$  is the fluid density (kg/m<sup>3</sup>);  $u_f$  is the velocity vector (m/s); p is fluid pressure (Pa);  $\mu$  is the dynamic viscosity (Pa·s);  $u_m$  is the coordinate velocity (m/s).

Blood is a non-Newtonian fluid whose viscosity is influenced by factors like hematocrit levels and plasma composition, but in large arteries with high shear rates (> 50 s<sup>-1</sup>), it behaves more like a Newtonian fluid due to red blood cell deformability [28]. Consequently, in this work, blood is modeled as an isotropic and incompressible Newtonian fluid with a density of 1060 kg/m³ and a viscosity of 0.0035 Pa·s [29]. The flow pattern is assessed based on calculations of the peak Reynolds number ( $Re_p$ ), Womersley number ( $\alpha$ ), and the critical Reynolds number ( $\alpha$ ) for transition to turbulence reported by Kousera et al. [31]. Given that the peak Reynolds number ( $\alpha$ ), the flow can be modeled as laminar flow.

## 2.2.2. Solid mechanics model

Based on Newton's Second Law, the momentum equation that describes the transient deformation of the vascular wall is as follows:

$$\rho_{s} \frac{\partial^{2} u_{s}}{\partial t^{2}} = \nabla \cdot (FS)^{T} + F_{v}$$
(2.3)

$$F = I + \nabla d_s \tag{2.4}$$

where  $\rho_s$  is the vascular wall density (kg/m³);  $u_s$  is the displacement vector (m);  $d_s$  is the displacement vector (m); F is the deformation gradient; F is the second Piola-Kirchhoff stress (N/m²);  $F_v$  is the volume force vector (N/m³); F is the identity matrix.

Due to the lack of in vivo data for the mechanical properties of PAU tissue materials, and given that Schussnig et al. [32] have demonstrated similar magnitudes of shear stress distributions predicted by various

vessel wall models, the arterial wall and PAU are modeled by assuming isotropic linear elasticity, having the same density, i.e.,  $1120~{\rm kg/m}^3$  [33]. Young's modulus and Poisson's ratio of the arterial wall are 1.08 MPa and 0.49, respectively [33]. As PAU is usually accompanied by atherosclerosis, based on the comparison of Young's modulus of atherosclerotic and normal vascular walls provided by a related study [34], Young's modulus of PAU is set to 3.00 MPa in this work. The Poisson's ratio of the PAU is 0.49. The above material properties are listed in Fig. 2.

#### 2.2.3. Fluid-structure interaction

The Arbitrary-Lagrangian-Eulerian formulation (ALE), as a hybrid technique, integrates the advantages of both Eulerian and Lagrangian methods. ALE is particularly effective in handling problems involving fluid-solid interfaces, offering robust solutions for such complex interactions [35]. At the fluid-solid interface, the surface of the vascular wall is subjected to forces exerted by the blood, as described:

$$F_T = -\mathbf{n} \cdot (-p\mathbf{I} + \mu(\nabla u_f + (\nabla u_f)^T)$$
(2.5)

where n is the normal vector of the boundary;  $F_T$  is the total force exerted on the vascular wall by the fluid (N); I is the identity matrix. In addition, at this interface, the following coupling conditions need to be satisfied:

$$d_{\rm s} = d_{\rm f} \tag{2.6}$$

$$\sigma_{s} \cdot n_{s} = \sigma_{f} \cdot n_{f} \tag{2.7}$$

where  $\sigma$ , n and d are the stress tensor, normal vector, and displacement vectors at the fluid-structure interface, respectively, with the subscripts s and f denoting the solid and fluid domains. We also have  $n_s = -n_f$  at this fluid-solid interface. A no-slip boundary condition is set at the fluid-solid interface.

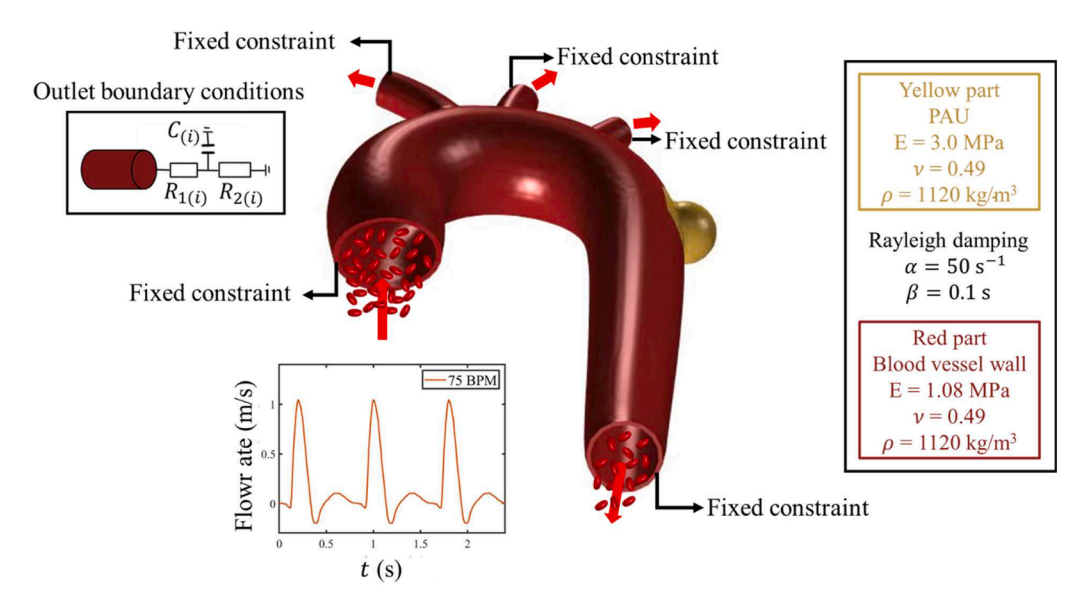


Fig. 2. Boundary and initial conditions (Red arrows indicate the direction of blood flow).

#### 2.3. Boundary and initial conditions

#### 2.3.1. Fluid domain

To simulate the pulsatile blood flow in the aorta, a physiological pulsating flow profile [33] is set at the inlet boundary (see Fig. 2). The pulsating flow includes phases of acceleration, deceleration, reverse flow, and zero flow, representing realistic cardiac cycle dynamics.

At the downstream end of the artery, the arterial branches are connected to a network of capillaries. To capture the impedance properties and vascular compliance of the aorta's downstream regions, Windkessel models are implemented at the outlet boundaries (see Fig. 2). The Windkessel model analogizes the cardiovascular system to an electrical circuit, where arterial compliance (the elasticity and distensibility of large arteries) is represented as a capacitor C; peripheral resistance (the resistance to blood flow through the arterial system) is represented as a resistor R; blood flow is represented as current Q; blood pressure in the aorta is represented as a time-varying potential p [36]. In this study, the impedance of the proximal vascular region is regarded as a resistor  $R_1$ , the impedance of the distal vascular region as a resistor  $R_2$ , and the compliance of the downstream blood vessel as a capacitor C. The mathematical description of the Windkessel model is as follows:

$$p_i = (R_{1(i)} + R_{2(i)})Q_i - R_{2(i)}C_i\frac{dp_i}{dt} + C_iR_{1(i)}R_{2(i)}\frac{dQ_i}{dt}$$
 (2.8)

where  $p_i$  is the pressure at outlet i and  $Q_i$  is the flow at outlet i. Accurately determining the parameter values for the Windkessel model is a challenging task, as it typically requires clinical measurements of transient blood flow and pressure from patients. However, since this work adopts an idealized model, a non-invasive method [37] is utilized to estimate these parameter values. The derived parameter values are summarized in Table 1. The detailed steps to get these parameter values are provided in the Supplementary Material S1.

**Table 1**The Windkessel model parameters. The values of capacitance *C* are taken from [38].

Outlet i	1 (BA)	2 (LCA)	3 (LSA)	4 (DA)
$R_1 (kg \cdot m^{-4} \cdot s^{-1})$ $C (m^4 \cdot s^2 \cdot kg^{-1})$ $R_2 (kg \cdot m^{-4} \cdot s^{-1})$	$\begin{array}{c} 4.08 \times 10^8 \\ 3.47 \times 10^{-7} \\ 2.60 \times 10^7 \end{array}$	$\begin{array}{c} 1.63 \times 10^9 \\ 1.64 \times 10^{-9} \\ 1.04 \times 10^8 \end{array}$	$\begin{array}{c} 1.33\times10^9\\ 2.12\times10^{-9}\\ 8.47\times10^7 \end{array}$	$\begin{array}{c} 1.20\times10^{8}\\ 1.59\times10^{-8}\\ 7.69\times10^{6} \end{array}$

#### 2.3.2. Solid domain

The terminal ends of the simulated aortic vessel are constrained to be immobile (see Fig. 2). In addition, considering the support of the periaortic tissue, Rayleigh damping [29] is applied to both the PAU and the vascular wall as follows (see Fig. 2):

$$\rho_{s} \frac{\partial^{2} u_{s}}{\partial t^{2}} + \alpha_{dM} \rho \frac{\partial u_{s}}{\partial t} = \nabla \cdot \left( (FS)^{T} + \beta_{dK} \frac{\partial (FS)^{T}}{\partial t} \right) + F_{v}$$
(2.9)

where  $\alpha_{dM}$  is the mass damping parameter (s<sup>-1</sup>),  $\alpha_{dM} = 50$  s<sup>-1</sup>;  $\beta_{dK}$  is the stiffness damping parameter (s),  $\beta_{dK} = 0.1$  s.

## 2.4. Numerical details

To facilitate convergence in this FSI calculation, fully coupled and direct solvers were employed. The computational domain was discretized using a hybrid mesh consisting of 157,736 elements including 109,880 tetrahedral elements and 47,856 prismatic boundary layer elements. More mesh details and mesh independence studies are provided in the Supplementary Material S2. The direct method (i.e., NUMPS) was adopted for the linear solution within the fully coupled solver. Automatic (Newton) was adopted for the nonlinear method in the fully coupled solver. Considering the balance between computational cost and solution accuracy, the maximum iterative times was set to 20. The time stepping was performed using a second-order backward difference formula with a fixed time step of 0.01 s, which was determined through a time-step independence study described in the Supplementary Material S2. To ensure stability in model cycle variation, the initial pressure was set to 70 mmHg, and a simulation spanning 8 cardiac cycles was conducted. Simulation results indicated that by the 6th cycle, the difference was below 2 %, indicating reach stability. Therefore, the 6th cycle was designated as the first cycle for analysis. The simulation was extended for two additional cycles, concluding at the end of the 8th cycle. The results from the 2nd cardiac cycle of this set of three cycles are presented and analyzed in the following sections. More details regarding the initialization process are provided in the Supplementary Material S3. In addition, to validate the rationality of the simulation results, a qualitative comparison between the simulation outcomes and clinical findings is presented in the Supplementary Material S4.

#### 3. Results & discussion

In this section, we first analyze a base case system involving a PAU

located laterally to the greater curvature of the aortic isthmus, which is the junction between the aortic arch and the descending aorta (see Fig. 2). For this base case, the interactions between the deformation of PAU-embedded blood vessels and blood flow dynamics are systematically and quantitatively analyzed. Subsequently, the effects of PAU size, blood pressure, and heart rate on the hemodynamics of PAUs at different locations are explored. These effects are quantified to assess how lowering blood pressure or heart rate can mitigate the risk of PAU progression and rupture. Finally, the hemodynamics of a single big PAU and two small PAUs are compared to determine which scenario presents a higher progression risk.

#### 3.1. Base case analysis

The boundary conditions and other parameters for the base case are shown in Fig. 2. The initial blood pressure and heart rate in the base case

are set to 85 mmHg and 75 BPM, respectively. The calculated pressure range at the inlet is 80/135 mmHg, which is recognized as hypertension according to the hypertension criterion ( $\geq 80/130$  mmHg). Fig. 3(a) shows a cross-sectional view of the evolution of the velocity distribution during the 2nd cardiac cycle (0.8-1.6 s). Pulsatile flow in the aorta is clearly observed, with the flow rate reaching its peak at t = 1.00 s during systole. Flow stagnation, attributed to secondary flow, is evident in the region of the PAU throughout the complete cycle. During systole, specifically at t = 1.00 s, a vortex can be clearly observed where blood flows from the lower neck region into the dome region of the PAU and then merges with the main aortic flow through the upper neck region (Fig. 3 (b)). The simulated flow pattern in the PAU aligns with clinical observations [39]. The slower blood flow in the PAU region may contribute to the PAU progression [26]. To quantitatively analyze the hemodynamics, biomechanical parameters such as WSS, von Mises stress, and displacement will be further evaluated.

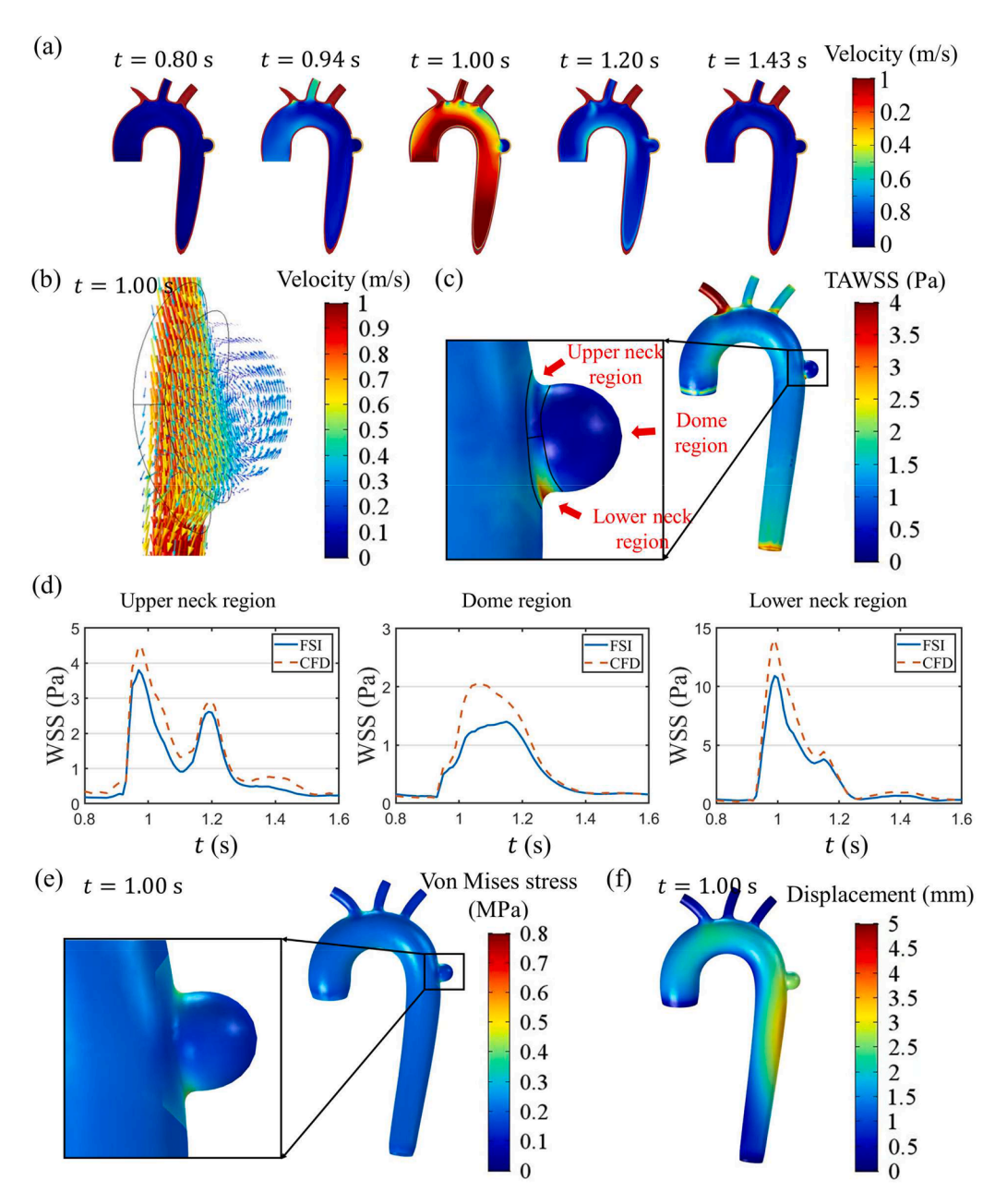


**Fig. 3.** FSI analysis for the base case. (a) cross-sectional velocity field during one cardiac cycle; (b) velocity field in the PAU region at t = 1.00 s; (c) the TAWSS distribution and in the segmented PAU region; (d) the comparison of WSS evolution over one cardiac cycle between FSI simulation and CFD simulation; (e) the von Mises stress distribution at t = 1.00 s; (f) the displacement distribution at t = 1.00 s.

Wall shear stress (WSS) is the tangential stress exerted by blood flow on the endothelial surface of the arterial wall. Endothelial cells in the vascular wall can detect changes in WSS, and deviations from the physiological WSS range (approximately 1.0–3.0 Pa [11]) can induce vascular wall remodeling [9,10]. The magnitude of WSS ( $\tau_w$ ) is determined by the velocity gradient of blood flow near the vascular wall and blood viscosity, as expressed by Newton's law of viscosity:

$$\tau_{w} = \mu \frac{\partial u_{p}}{\partial x_{n}} \tag{3.1}$$

where  $\frac{\partial u_p}{\partial x_n}$  is the shear rate or velocity gradient at the vascular wall. Time-averaged wall shear stress (TAWSS) represents a key hemodynamic metric for assessing the progression and rupture risks of PAUs, which is defined as:

$$TAWSS = \frac{1}{T} \int_{t}^{t+T} |\tau_{w}| dt$$
 (3.2)

where T denotes the duration of a cardiac cycle. The physiological WSS range of 1.0–3.0 Pa was adopted as the reference standard in this study. Fig. 3(c) illustrates the distribution of TAWSS for the base case by FSI analysis during the 2nd cardiac cycle, which can be further areaaveraged to estimate the regional TAWSS. As shown in Fig. 3(b) and (c), the presence of a vortex in the PAU region resulted in low TAWSS in the PAU dome (0.54 Pa), contrasting with the high TAWSS observed in the upper neck (1.02 Pa) and lower neck (2.13 Pa) regions. Notably, the TAWSS in the dome region fell below the physiological range, indicating potential risks of PAU progression and rupture. In the PAU neck region, which is typically characterized by the presence of atheromatous calcified plaques [40,41], high TAWSS may contribute to the destabilization of atherosclerotic plaques. Although the TAWSS in the neck region for the base case remained within the physiological range, other varying conditions may lead to deviations beyond the physiological range, as observed in our parametric study. Therefore, it is essential to quantify localized WSS at different regions of PAU, i.e., the dome, upper neck and lower neck regions.

A comparative analysis was conducted between CFD simulations, which assume rigid wall conditions, and FSI simulations. The FSI simulations account for the displacement and expansion of the aortic wall induced by blood pressure, resulting in lower WSS values across all three regions of the PAU compared to CFD predictions (Fig. 3(d)). Lower WSS increases intercellular permeability, thereby enhancing vascular wall fragility, potentially contributing to PAU progression and rupture [26]. Thus, overestimation of WSS by neglecting blood vessel wall deformation (an intrinsic limitation of CFD simulations alone) may lead to erroneous conclusions regarding PAU progression and rupture risks. Moreover, elevated blood pressure can induce excessive tissue stress (von Mises stress) in the vascular wall, which may directly contribute to PAU rupture [42]. The FSI method allows for the calculation of von Mises stress and displacement of the solid domain, specifically the vascular wall and PAU, which are critical biomechanical parameters that cannot be captured through CFD simulations alone.

Fig. 3(e) illustrates the distribution of von Mises stress at  $t=1.00\,\mathrm{s}$  during systole for the base case. The von Mises stress, also known as wall effective stress [13], is a widely utilized metric for evaluating material failure. It is given as:

$$\sigma_{e} = \sqrt{\frac{1}{2} \sum_{(i, j)} \left[ \left( \sigma_{ii} - \sigma_{jj} \right)^{2} + 6\sigma_{ij}^{2} \right]}, \quad (i, j) \in \{ (x, y), (x, z), (y, z) \}$$
(3.3)

where  $\sigma_{ij}$  is the Cauchy stress component in the solid material (i.e., the vascular wall or PAU). Some studies have employed von Mises stress as a metric for evaluating the rupture risk of aortic diseases [13,22,29]. Results in Fig. 3(e) show that the von Mises stress in the neck region is relatively higher than in the dome region. However, it is important to

note that this observation alone does not conclusively indicate a higher rupture propensity in the neck region compared to the dome. This is because the dome region exhibits lower TAWSS than the neck region, making the dome region more fragile. Consequently, a comprehensive evaluation of PAU rupture risk necessitates the integration of both TAWSS and von Mises stress analyses to account for the complex interplay between hemodynamic and structural factors.

Fig. 3(f) illustrates the distribution of displacement at  $t=1.00~\rm s$  during systole for the base case. It shows that the centrifugal forces generated by the curvature of the aortic arch result in greater deformation on the greater curvature of the aorta, leading to significant deformation of the PAU in the base case.

#### 3.2. The effects of PAU location, PAU size, blood pressure, and heart rate

#### 3.2.1. The effect of PAU location

PAUs can occur at various locations along the thoracic aorta, with their locations potentially influencing the selection of clinical treatment strategies. Therefore, assessing the effect of PAU location on disease risks is of great importance. In this work, there are five locations of PAUs considered as illustrated in Fig. 4(a):

Location I: Located in the aortic arch.

Location II: Located lateral to the lesser curvature of the aortic isthmus.

Location III: Located lateral to the greater curvature of the aortic isthmus.

Location IV: Located lateral to the lesser curvature of the descending aorta.

Location V: Located lateral to the greater curvature of the descending aorta.

Fig. 4(a) illustrates the distribution of TAWSS for different locations of PAUs. It shows that, in the dome region, the TAWSS values of PAUs at Location II (0.84 Pa), Location III (0.54 Pa), Location IV (0.87 Pa), and Location V (0.87 Pa) are significantly lower compared to Location I (1.39 Pa). Notably, for the former four, the TAWSS in the dome region is below the physiological range, which implies a high susceptibility to PAU progression. This result provides a hemodynamic explanation for the clinical predominance of PAU occurrence in the descending aorta.

In addition, our results show that the TAWSS in the neck region of PAU at Location I is notably higher than the other four locations (Fig. 4 (a)). Specifically, the TAWSS in the lower neck of PAU at Location I is 3.67 Pa, exceeding the physiological range, whereas the TAWSS values at the other four locations are significantly lower: 2.88 Pa (Location II), 2.13 Pa (Location III), 3.13 Pa (Location IV), and 3.30 Pa (Location V) (Fig. 4(a)). This suggests an increased vulnerability to plaque rupture for PAUs at Location I, which is particularly concerning given their anatomical proximity to cerebral vasculature. The potential clinical implications are severe, as plaque rupture in this region could precipitate catastrophic cerebrovascular events, including cortical or subcortical infarction [43]. Such events pose significant risks of life-threatening brain tissue damage. Therefore, prompt therapeutic intervention, such as emergency surgery, is especially important for PAUs located at the aortic arch. Also, as shown in Fig. 5(b), PAUs at Location I exhibit higher von Mises stress compared to other locations. It indicates that PAUs in the aortic arch are at heightened risk of acute rupture, further underscoring the critical importance of prompt therapeutic intervention.

## 3.2.2. The effect of PAU size

To investigate the effect of PAU size on its progression and rupture risks, we conducted a parametric analysis by scaling the PAU size from the base case. In addition to the base case (r=8 mm, referred to as 'middle'), PAU sizes of r=6 mm (referred to as 'small') and r=10 mm (referred to as 'big') were considered, respectively (Fig. 4(b)).

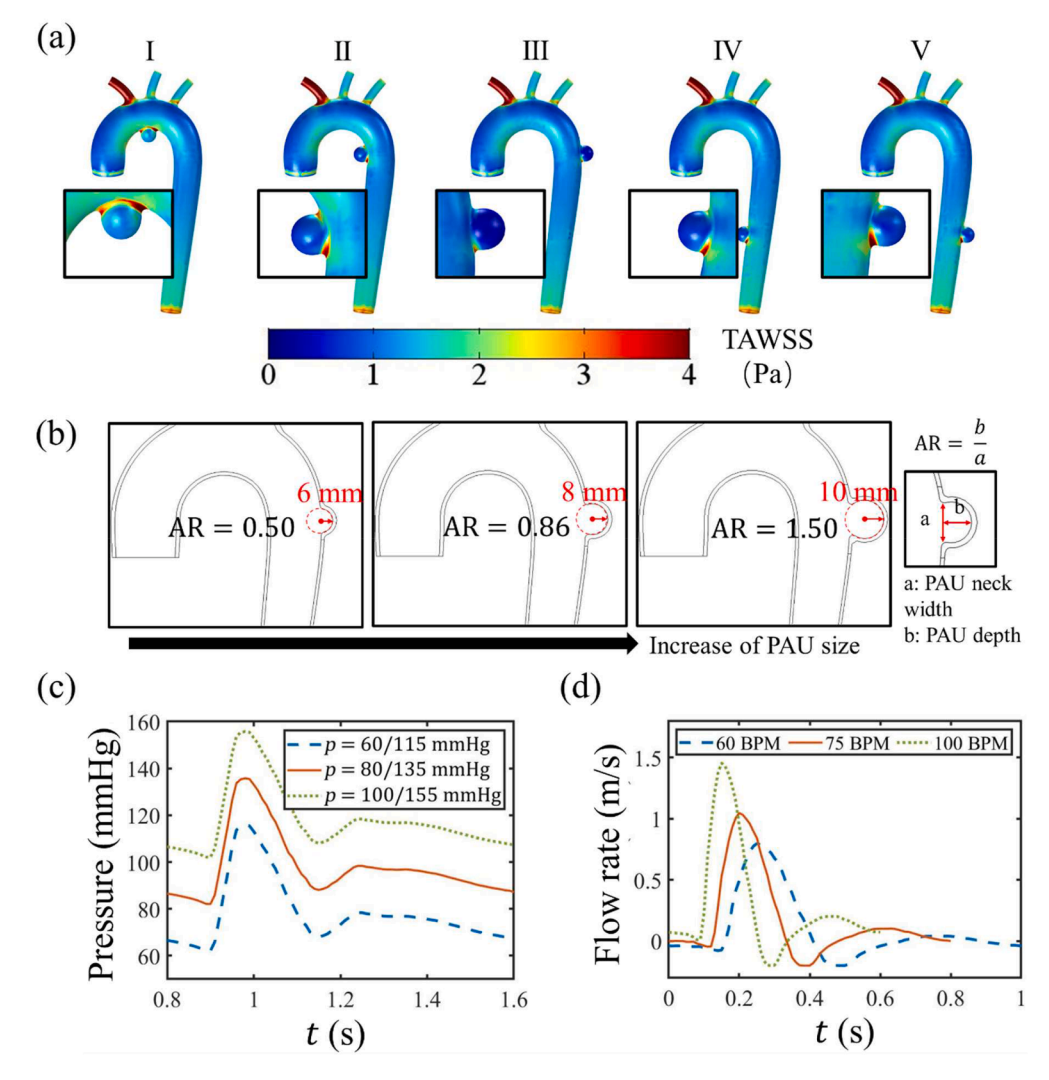


Fig. 4. Settings for different conditions. (a) the TAWSS distributions for five locations of PAUs; (b) cross-sectional view of aortic isthmus PAUs of different sizes; (c) the evolution of different inlet pressures over one cardiac cycle (0.8–1.6 s); (d) the evolution of different heart rates over one cardiac cycle.

Additionally, larger PAUs generally have a larger aspect ratio (AR) [2], which is defined as the ratio of PAU depth to its neck width. The AR values for different-sized PAUs ( $r=6~\mathrm{mm}$ ,  $r=8~\mathrm{mm}$ , and  $r=10~\mathrm{mm}$ ) are 0.50, 0.86, and 1.50, respectively, as depicted in Fig. 4(b).

Fig. 5(a) illustrates the distribution of TAWSS for different-sized PAUs at different locations. It shows that with an increase in PAU size, the TAWSS in the dome region decreases (see the red solid line in Fig. 6) regardless of the PAU location. Specifically, with the increase of PAU size, at Location I, the TAWSS in the dome region decreases from 1.42 Pa to 1.39 Pa and subsequently to 0.99 Pa (Fig. 6(a)Fig. 5. Stress distributions for PAUs at different locations and under different conditions. (a) the TAWSS distribution for different-sized PAUs located at different locations; (b) the von Mises stress distribution in the PAU regions under different blood pressures; (c) the TAWSS distribution in the PAU regions under different heart rates.). Similarly, at Location III, the TAWSS in the dome region decreases from 0.74 Pa to 0.54 Pa and then to 0.38 Pa (Fig. 6(c)), and at Location V, from 1.13 Pa to 0.87 Pa and further to 0.50 Pa (Fig. 6(e)). This reduction in TAWSS can be attributed to the increased volume of the PAU dome, which creates more extensive flow stagnation zones. Notably, as PAU size increases from 6 to 10 mm, the magnitude of TAWSS in the dome region progressively deviates from the physiological range (1.0-3.0 Pa). TAWSS values falling below the physiological range are associated with a higher risk of PAU progression [8,26]. Therefore, larger PAUs are associated with higher risks of PAU

progression and rupture.

#### 3.2.3. The effect of blood pressure

Clinically, hypertension represents a prevalent comorbidity in PAU patients and serves as a significant predisposing factor for PAU rupture. Consequently, conservative treatment focuses on blood pressure management, with  $\beta$ -blockers emerging as the primary pharmacological intervention [44]. Building on this clinical foundation, our study incorporates a comprehensive hemodynamic analysis to investigate the effect of different blood pressure levels on PAU progression and rupture risks. Alongside the base case (p=80/135 mmHg, referred to as 'middle'), two additional conditions are considered: hypertension (p=100/155 mmHg, referred to as 'big') and lower blood pressure (p=60/115 mmHg, referred to as 'small'), as illustrated in Fig. 4(c).

The hemodynamic analysis reveals that elevated blood pressure induces vascular wall and PAU dilatation, consequently reducing the velocity gradient proximal to the vascular surface. This can result in a slight decrease in TAWSS, though the magnitude of this decrease is not significant (see the purple dashed line in Fig. 6). For instance, for the PAU at Location III, the TAWSS in the dome region decreases from 0.56 Pa to 0.54 Pa and subsequently to 0.52 Pa with increasing pressure, and in the upper neck region, it decreases from 1.05 Pa to 1.02 Pa and then to 1.00 Pa (Fig. 6(c)). However, for PAUs at Locations I and II, the TAWSS in the dome shows a slight decrease when blood pressure increases from

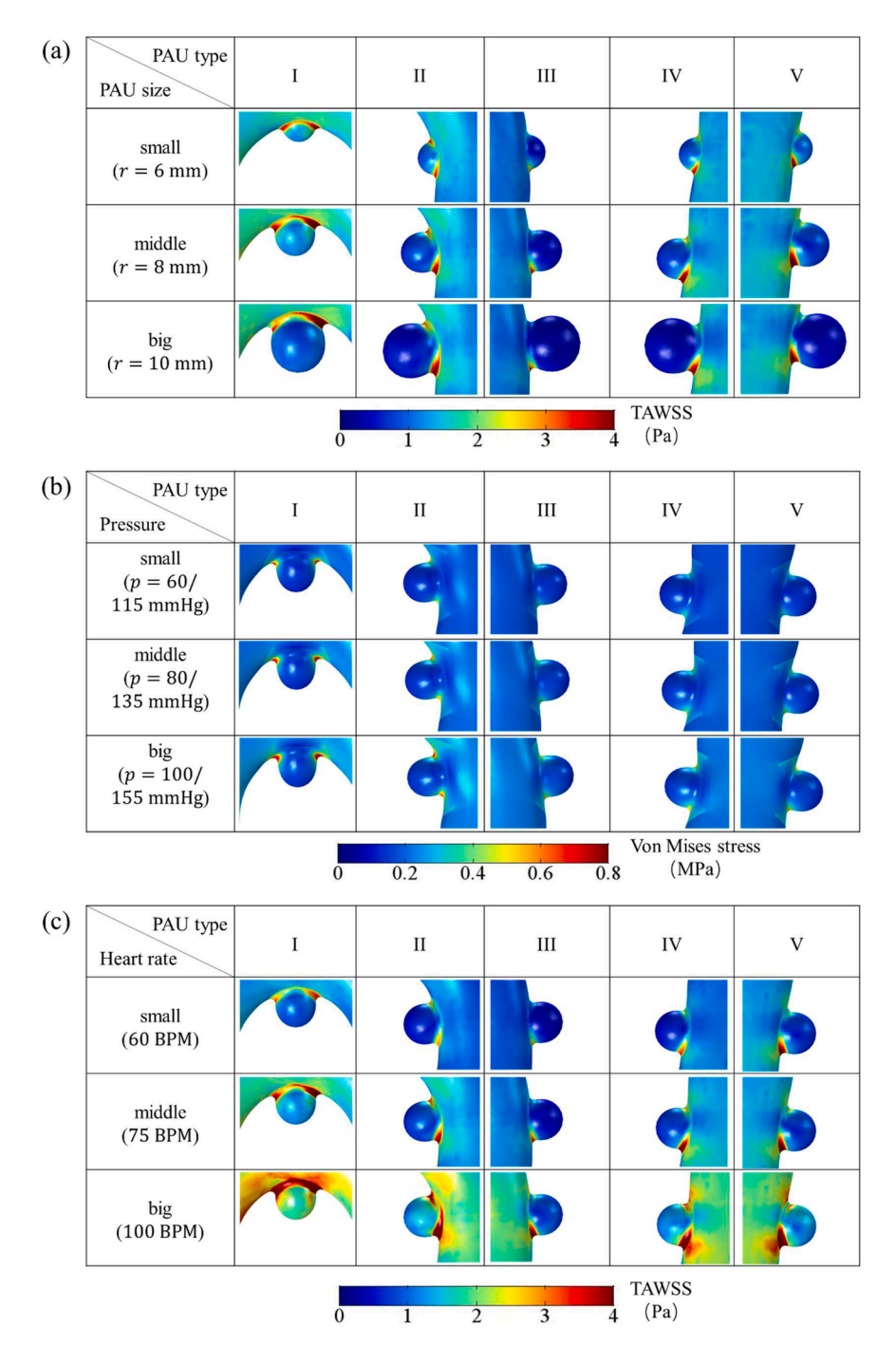


Fig. 5. Stress distributions for PAUs at different locations and under different conditions. (a) the TAWSS distribution for different-sized PAUs located at different locations; (b) the von Mises stress distribution in the PAU regions under different blood pressures; (c) the TAWSS distribution in the PAU regions under different heart rates.

60/115 mmHg to 80/135 mmHg, but then increases slightly when pressure increases from 80/135 mmHg to 100/155 mmHg (Fig. 6(a) and (b)). This phenomenon can be attributed to the competing hemodynamic effects of elevated pressure: while increased vascular displacement tends to reduce the velocity gradient, the concomitant enhancement of vortex flow within the PAU cavity can partially counteract this effect. When the vortex-induced flow acceleration surpasses the displacement effect, a net increase in velocity gradient occurs. Overall, blood pressure fluctuations within the investigated range exert minimal impact on TAWSS magnitude across all PAU locations.

Fig. 5(b) demonstrates the von Mises stress distribution under different pressure conditions for PAUs at different locations. The results

reveal a significant positive correlation between blood pressure elevation and von Mises stress elevation, particularly in the neck region. For instance, for the PAU at Location I, the von Mises stress in the upper neck region increases from 0.30 MPa under the lower blood pressure condition ( $p=60/115~{\rm mmHg}$ ) to 0.40 MPa under the hypertension condition ( $p=100/155~{\rm mmHg}$ ) (Fig. 7(a)). Similarly, for the PAU at Location IV, the von Mises stress in the lower neck region rises from 0.17 MPa ( $p=60/115~{\rm mmHg}$ ) to 0.22 MPa ( $p=80/135~{\rm mmHg}$ ) and further to 0.26 MPa ( $p=100/155~{\rm mmHg}$ ) (Fig. 7(d)). Please refer to the purple dashed line in Fig. 7 for more data. Therefore, these observations show that elevated blood pressure significantly increases the von Mises stress on PAU walls, thereby increasing the rupture risk.

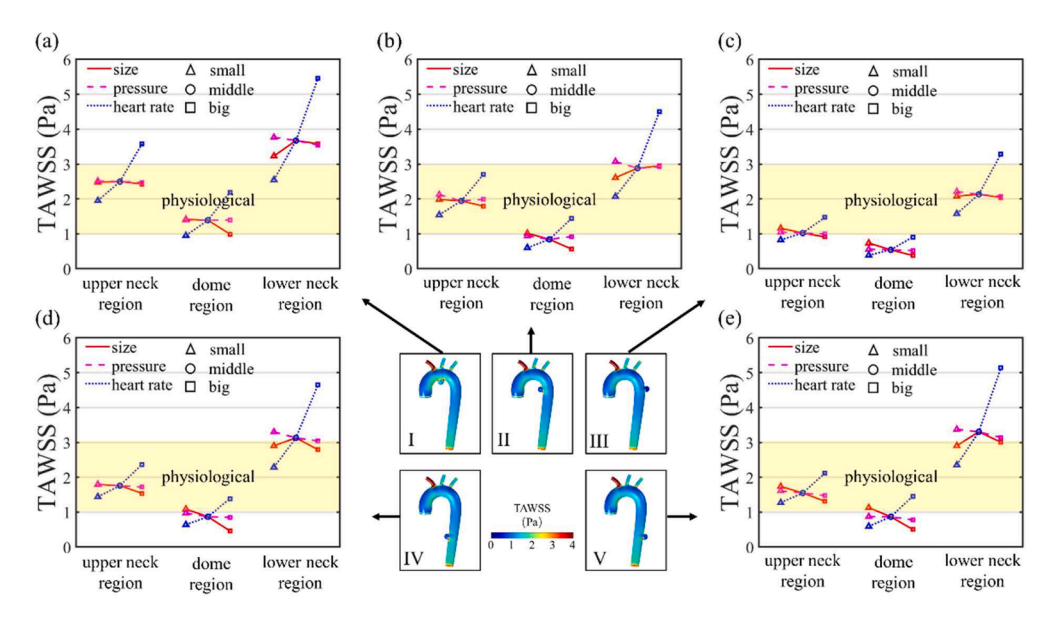


Fig. 6. The evolution of TAWSS under different conditions for PAUs at five locations. (a) Location I; (b) Location II; (c) Location III; (d) Location IV; (e) Location V.

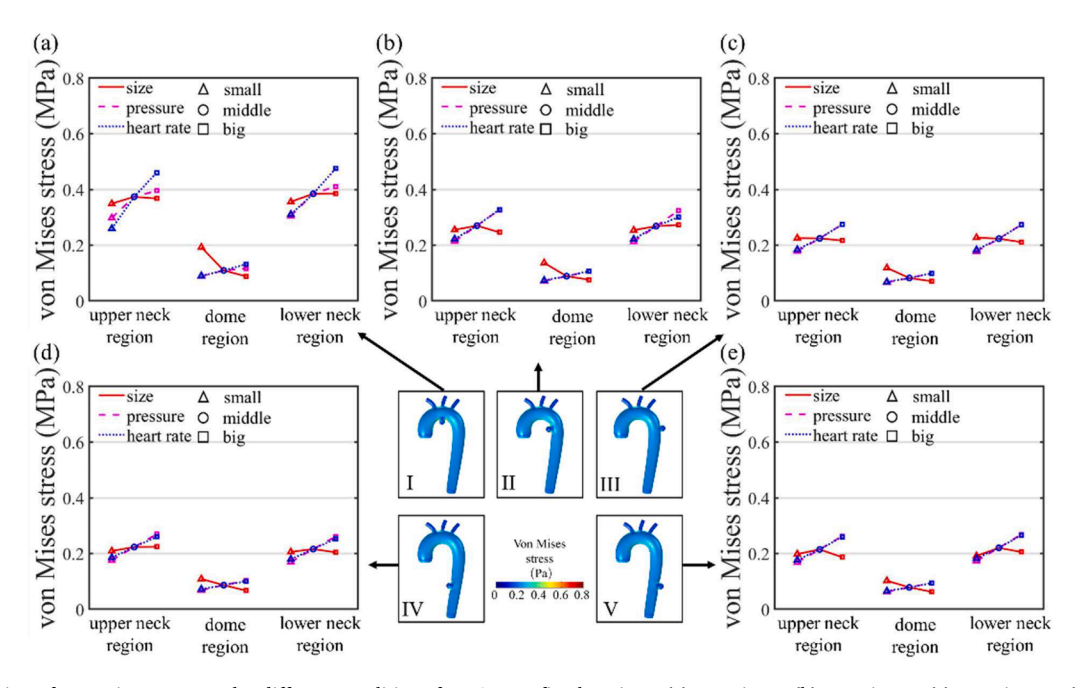


Fig. 7. The evolution of von Mises stress under different conditions for PAUs at five locations. (a) Location I; (b) Location II; (c) Location III; (d) Location IV; (e) Location V.

In addition, the purple dashed lines in Fig. 8 clearly demonstrate that increasing pressure levels significantly amplify the displacements of PAUs. For example, for the PAU at Location II, as pressure increases, the displacement in the dome region increases from 0.89 mm to 1.27 mm and then to 1.69 mm. Similarly, the displacement in the upper neck region from 1.06 mm to 1.40 mm and further to 1.76 mm, and in the lower neck region from 1.23 mm to 1.63 mm and ultimately to 2.08 mm (Fig. 8(b)). This result demonstrates that hypertension induces elevated mechanical deformation in PAU structures, thereby increasing the risk of PAU rupture.

## 3.2.4. The effect of heart rate

Clinically, an elevated heart rate is a significant risk factor for cardiovascular disease. Specifically, for PAU patients, heart rates exceeding 90 BPM have been demonstrated to increase the disease risks [45]. Fig. 4

(d) demonstrates three different heart rate conditions: 60 BPM (referred to as 'small'), 75 BPM (referred to as 'middle'), and 100 BPM (referred to as 'big'), with 75 BPM serving as the base case setting. The net amount of blood supplied by the heart per cycle remains the same [46] for all heart rate cases.

Fig. 5(c) shows that the TAWSS in the neck region increases with higher heart rates for all PAUs at different locations. For example, for the PAU at Location I, the TAWSS in the upper neck region is 1.95 Pa at a heart rate of 60 BPM, and rises to 3.58 Pa when the heart rate increases to 100 BPM (Fig. 6(a)); for the PAU at Location V, at heart rates of 60, 75, and 100 BPM, respectively, the TAWSSs in the lower neck region are 2.35 Pa, 3.30 Pa, and 5.14 Pa (Fig. 6(e)). For additional data, please refer to the blue dotted line in Fig. 6. This trend indicates that as the heart rate increases, the TAWSS in the lower neck region may gradually exceed the physiological range (1.0–3.0 Pa), with the implication of a greater risk of

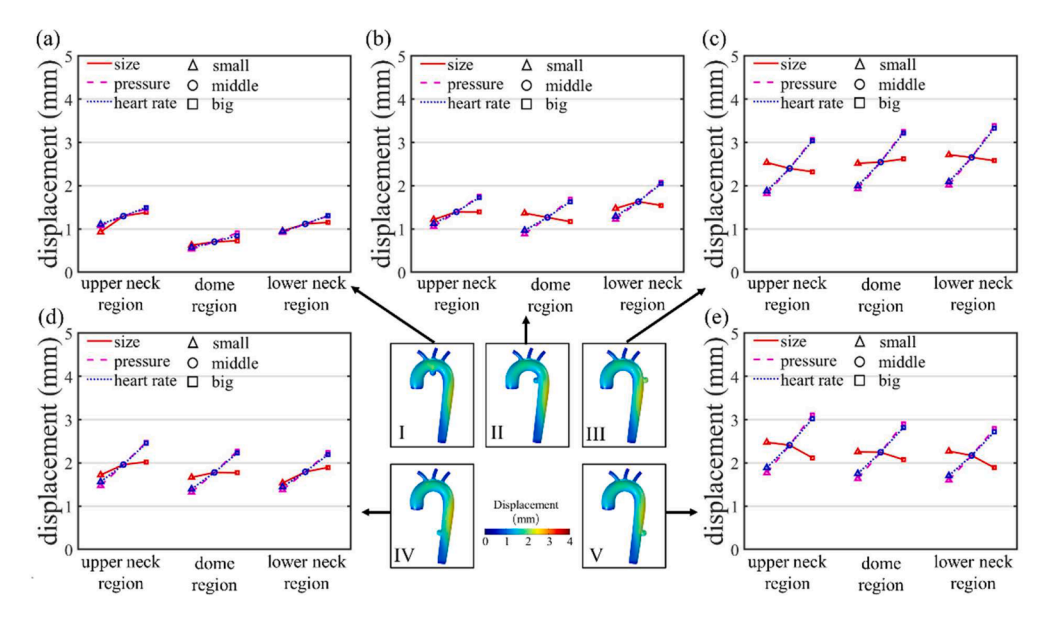


Fig. 8. The evolution of wall displacement under different conditions for PAUs at five locations. (a) Location I; (b) Location II; (c) Location III; (d) Location IV; (e) Location V.

ulcerated plaque rupture. In addition, it is found that as the heart rate increases to 100 BPM, the TAWSS in the PAU dome region increases to within the physiological range (1.0–3.0 Pa) (Fig. 6), which implies that proper exercise (which can elevate heart rate) could potentially help mitigate the PAU progression to some extent.

Blue dotted lines in Figs. 7 and 8 show that an increase in heart rate is associated with higher von Mises stress and displacement for PAUs at all locations. This can be attributed to the elevated peak velocity during the cardiac cycle resulting from an increased heart rate, which leads to a greater impact of blood flow on the vessel wall. Therefore, A higher heart rate is associated with a higher rupture risk of PAU.

# 3.2.5. Correlation analysis of PAU size, pressure, and heart rate on hemodynamic parameters

To quantify the effects of PAU size, blood pressure, and heart rate on each hemodynamic parameter, a regression analysis is conducted. Specifically, least squares regression is employed to estimate the slopes (*k*) of all lines in Figs. 6–8 according to the following equation:

$$k = \sum_{i=1}^{n} (x_i - \overline{x})(y_i - \overline{y}) / \sum_{i=1}^{n} (x_i - \overline{x})^2$$
 (3.4)

where  $y_i$  represents the values of TAWSS, von Mises stress, and displacement under a specific condition,  $x_i$  represents the normalized values of these biological factors (PAU size, blood pressure, and heart rate), and k represents the influence magnitude of x on y. The symbols  $\overline{y}$  and  $\overline{x}$  denote the averages of  $y_i$  and  $x_i$  respectively. To enable comparative analysis of the effects of biological factors on different biomechanical parameters, all variables were normalized using the following equation:

$$x_i = (a_i - a_{min})/(a_{max} - a_{min}) \tag{3.5}$$

where  $a_i$  represents the value of each biological factor, with diastolic pressure specifically employed for blood pressure quantification. The normalization ranges were established based on physiological extremes: for PAU size,  $\alpha_{max}$  and  $\alpha_{min}$  are set to 20 mm and 0 mm respectively; for blood pressure,  $\alpha_{max}$  and  $\alpha_{min}$  are set to 240 mmHg and 0 mmHg respectively; for heart rate,  $\alpha_{max}$  and  $\alpha_{min}$  are set to 220 BPM and 0 BPM respectively.

To quantitatively compare these effects, we further normalized the slopes (*k*) of TAWSS, von Mises stress, and displacement, by introducing

a dimensionless correlation factor (R):

$$R = k/\max|k| \tag{3.6}$$

Fig. 9 illustrates the correlation factors (R) for all PAUs at five locations in this work. It is understandable that R>0 indicates a positive correlation, while R<0 indicates a negative correlation. Additionally, the absolute value of R reflects the strength of the association. We specify that R>0.2 indicates a significant positive influence and R<-0.1 indicates a significant negative influence in this work. For example, for the PAU at Location I, the correlation factor (R) of PAU size on TAWSS in the dome region is -0.13 (see the first row and the second column in Fig. 9), which indicates a significant reduction in TAWSS with increasing PAU size; and for the PAU at Location III, the R of pressure on von Mises stress in the upper neck region is 0.54 (see the eighth row and the fourth column in Fig. 9), which indicates that the von Mises stress experiences a significant increase with the increase of pressure.

In Fig. 9, it can be observed that rows 1–5 in column 2 all have *R*-values below –0.1, which demonstrates that an increase in PAU size primarily contributes to a reduction in TAWSS in the dome region. Moreover, it can be observed that rows 6–15 in columns 4–9 almost all have *R*-values exceeding 0.2, which demonstrates that increasing blood pressure significantly increases von Mises stress and displacement. Additionally, it can be observed that rows 1–5 in columns 7 and 9 have *R*-values exceeding 0.2, which indicates that an increased heart rate predominantly affects the increase in TAWSS in the neck regions. In conclusion, Fig. 9 elucidates the effects of various factors on different biomechanical metrics, thereby enabling us to evaluate how the regulation of these factors can influence the progression and rupture risks of PAU.

Clinically adopted conservative therapy, which focuses on reducing blood pressure and heart rate, should be a strategy for managing PAU. We found that reducing blood pressure and heart rate can lead to a significant decrease in von Mises stress and displacements which may mitigate the risk of PAU rupture. However, our findings also suggest that reducing blood pressure and heart rate does not significantly increase the TAWSS in the dome region of PAU, which is necessary to mitigate the risk of PAU progression. In Fig. 9, it can be observed that rows 1–5 in columns 4–6 have -0.1 < R < 0, which demonstrates that reducing blood pressure only leads to a very slight increase of the TAWSS in the PAU region. This limitation may contribute to the unfavorable outcomes commonly observed in the natural prognosis of clinically PAUs.

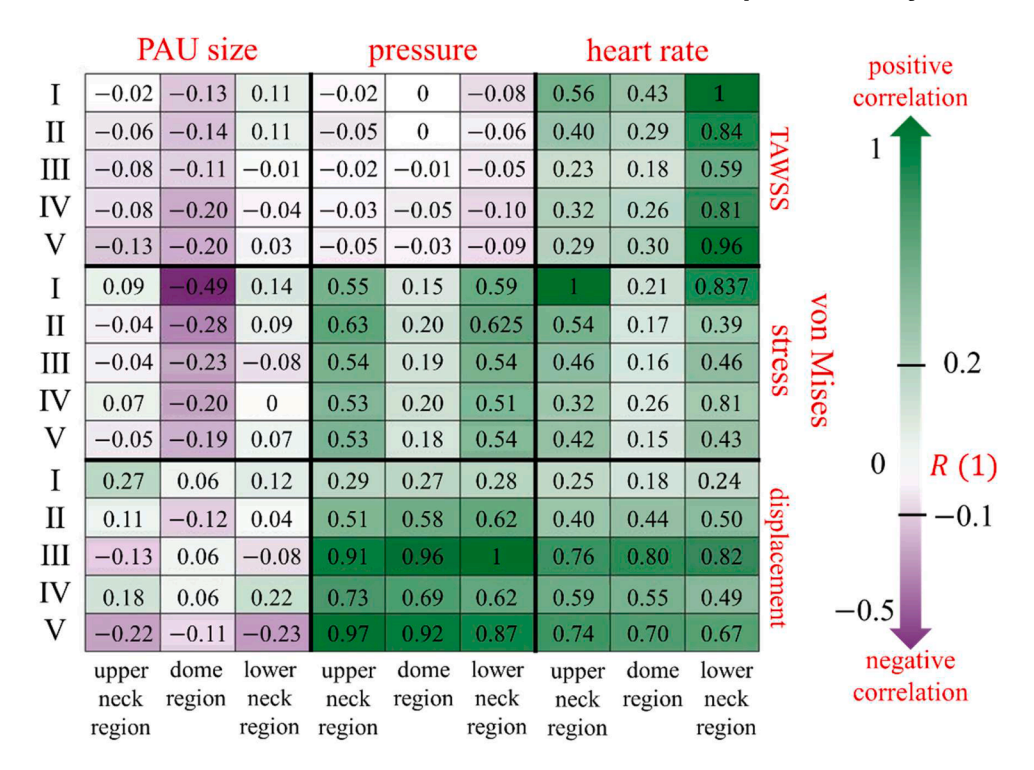


Fig. 9. R values showing the influence of PAU size, blood pressure, and heart rate on hemodynamic parameters for PAUs at different locations by correlation analysis.

## 3.3. Risk comparison between a single big PAU and two small PAUs

In the previous sections, we analyzed the hemodynamics of a single PAU and systematically investigated the effects of PAU location, size, blood pressure, and heart rate on PAU progression and rupture risks. However, clinical presentations often involve more complex scenarios, particularly multiple PAUs. This raises a crucial clinical question: Which scenario poses a higher risk—multiple small PAUs or a single big PAU? In this study, we controlled the total volume of PAUs to be the same and examined two scenarios: one case with a single big PAU ( $r=8.00~\mathrm{mm}$ ) and the other case with two small PAUs ( $r=5.65~\mathrm{mm}$ ) (Fig. 10). These configurations were compared to evaluate their relative progression risks.

Fig. 10 shows the distributions of TAWSS for two small PAUs versus a single big PAU at various locations. Both scenarios exhibit low TAWSS in

the dome region and high TAWSS in the neck region. Fig. 11 provides a quantitative comparison of the TAWSS values in different regions for a single big PAU and two small PAUs. Notably, at all five locations, the TAWSS of two small PAUs is closer to the physiological range than that of a single big PAU (Fig. 11). Focusing on TAWSS values outside the physiological range, at Location I, the single big PAU has significantly higher TAWSS in the lower neck region compared to the two small PAUs, suggesting a higher risk of ulcer plaque rupture. Furthermore, at Locations II, III, IV, and V, in the dome region, the single big PAU exhibits significantly lower TAWSS than the two small PAUs, indicating a higher risk of progression (Fig. 11).

Through a comprehensive quantitative analysis of TAWSS distributions (Fig. 11), we compared hemodynamic characteristics between a single big PAU and two small PAUs. This study specifically addresses the clinical scenario of asymptomatic presentations, where the immediate

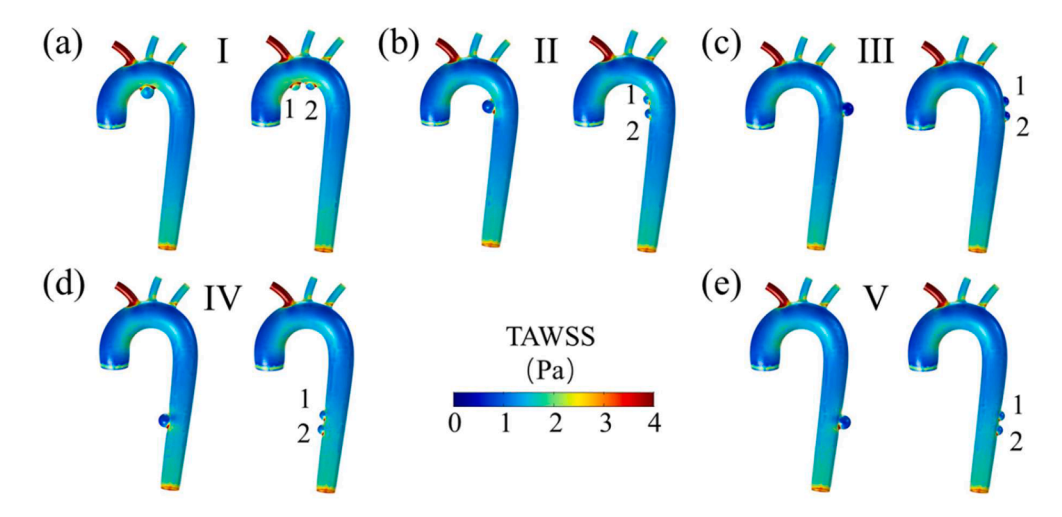


Fig. 10. The TAWSS distributions of a single big PAU and two small PAUs at five locations. (a) Location I; (b) Location II; (c) Location III; (d) Location IV; (e) Location V.

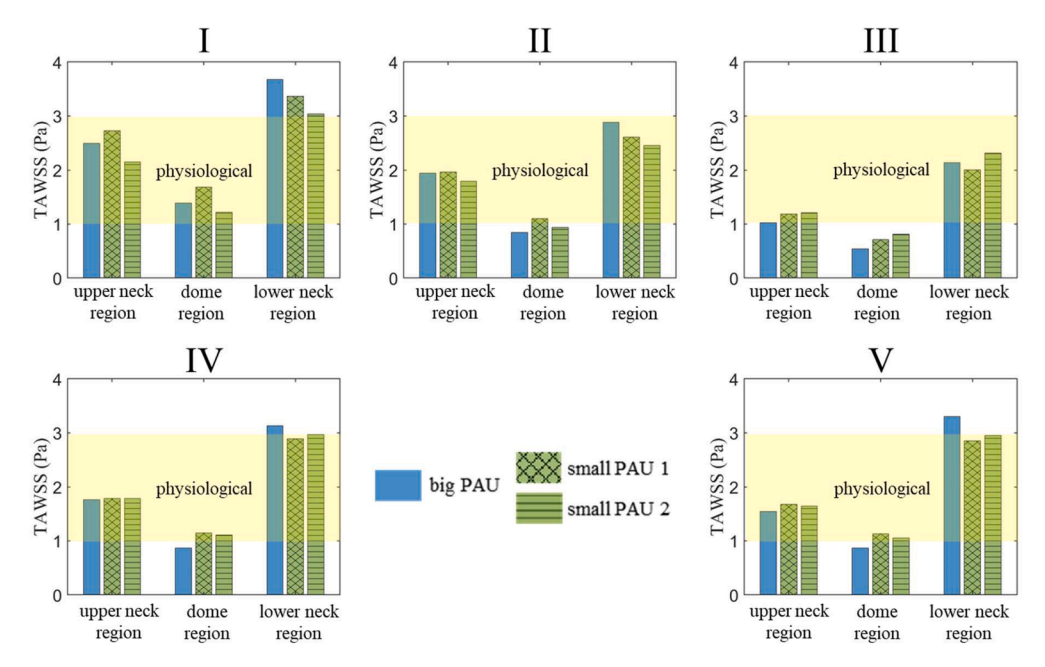


Fig. 11. The TAWSS values of a single big PAU and two small PAUs at five locations.

risk of rupture is minimal but monitoring progression is crucial. The analysis reveals that the big PAU exhibits a lower TAWSS in the dome region, suggesting that a single big PAU carries a higher progression risk compared to two small PAUs. It is crucial to emphasize that our findings specifically pertain to early-stage asymptomatic PAUs, where the structural integrity of the vessel wall remains relatively preserved, and both von Mises stress and displacements remain substantially below rupture thresholds. Therefore, von Mises stress and displacement were not quantitatively analyzed. However, in cases approaching rupture, where the PAU wall is commonly significantly thinner and more fragile, von Mises stress and displacement become critical determinants of rupture, warranting investigation in future studies.

## 4. Conclusions

A 3-dimensional PAU model considering the interaction between blood vessel wall deformation and blood flow dynamics has been developed in this work. Our model incorporates the impedance and compliance of the aorta by employing the Windkessel models at all outlet boundaries. Our analysis of the base case reveals that a low TAWSS in the dome region correlates with increased risks of PAU progression and rupture. Furthermore, high TAWSS in the neck region is linked to an elevated risk of ulcerated plaque rupture.

We compared model predictions from FSI simulations with those from CFD simulations. The FSI approach, which accounts for the interaction between blood flow and vascular wall deformation, produces lower WSS than CFD. Additionally, FSI provides valuable biomechanical parameters, such as von Mises stress and wall displacement. Low WSS can increase the vulnerability of the PAU wall, potentially leading to PAU progression or even rupture, while higher von Mises stress may result in immediate material failure, causing PAU rupture. Thus, FSI provides superior reliability in assessing PAU progression and rupture risks.

Moreover, our study conducted a comprehensive evaluation of the effect of biological factors, including PAU location and size, as well as blood pressure and heart rate on critical biomechanical metrics. The analysis yielded several significant findings: PAUs in the descending aorta exhibited lower TAWSS in the dome region compared to other locations, indicating an elevated progression risk; a progressive reduction in TAWSS was observed in the PAU dome region as the PAU radius

increased to 10 mm, with values falling below the physiological range (1.0–3.0 Pa), which suggested that the PAU progression and rupture risks increase with the growth of PAU size; elevated blood pressure and increased heart rate were both associated with higher von Mises stress and greater displacement, indicating an elevated risk of PAU rupture. Furthermore, correlation analysis demonstrated that reduced pressure and heart rate could decrease the von Mises stress and displacement of PAUs, thereby mitigating the rupture risk. However, this therapeutic approach failed to restore TAWSS in the dome region to the physiological range to halt PAU progression. Therefore, these findings provide quantitative biomechanical evidence supporting the limitations of conservative treatment strategies for PAUs

Additionally, the progression risk of a single big PAU was compared with that of two small PAUs with the same total volume, which is a common concern raised by clinicians. The results indicate that, in asymptomatic cases, a single large PAU presents a higher progression risk, thus requiring greater attention.

This work will facilitate clinicians in making well-informed decisions and increase the success of management for PAU diseases. Moreover, this study highlights the promising potential of FSI simulations in the diagnosis and treatment of aortic diseases.

However, several limitations of this study should be acknowledged. Firstly, the idealized aortic model does not fully capture the anatomical and structural characteristics of individual patients, potentially restricting the direct application of the findings in clinical practice. Secondly, the material properties of the arterial wall and PAU were assumed to be isotropic linear elastic materials. This assumption deviates from the actual biological tissues, which exhibit nonlinear and anisotropic properties. Consequently, this discrepancy may influence the accurate assessment of vessel wall stress and deformation. Additionally, blood was modeled as an incompressible Newtonian fluid, which may not fully account for the complex hemodynamic features in detail.

Future work will focus on utilizing patient-specific geometries and incorporating more realistic models for blood and the arterial wall. Given these biomechanical metrics influence aortic disease progression through pathobiological mechanisms, the development of pathologically relevant models and their integration with FSI simulations is of significant interest. However, more complex models inevitably demand higher computational costs. Therefore, we will also focus on model

optimization and accelerated computational methods to improve computational efficiency. We anticipate that these advancements will enable clinicians to tailor treatments more precisely to individual patients, thereby promoting personalized care.

#### **Ethics statement**

This study involves computational simulations and does not include any in vivo human or animal experiments. Therefore, no ethics approval was required for this research.

#### CRediT authorship contribution statement

**Tian Wu:** Investigation, Validation, Data curation, Writing – review & editing, Writing – original draft, Methodology, Visualization, Software, Formal analysis. **Hong Zhu:** Methodology, Writing – review & editing, Formal analysis. **Haoyu Zhuo:** Methodology, Investigation, Visualization. **Jiang Li:** Formal analysis, Writing – review & editing, Conceptualization. **Jie Xiao:** Methodology, Funding acquisition, Project administration, Conceptualization, Writing – review & editing, Supervision, Formal analysis, Investigation.

#### Declaration of competing interest

The authors declare that they have no known competing financial interests or personal relationships that could have appeared to influence the work reported in this paper.

#### Acknowledgements

We are grateful for the financial support from the National Natural Science Foundation of China (21978184), the "Jiangsu Innovation and Entrepreneurship (Shuang Chuang) Program", the "Jiangsu Specially Appointed Professors Program", and the "Priority Academic Program Development (PAPD) of Jiangsu Higher Education Institutions".

## Supplementary materials

Supplementary material associated with this article can be found, in the online version, at doi:10.1016/j.cmpb.2025.108973.

#### References

- E. Bossone, K.A. Eagle, Epidemiology and management of aortic disease: aortic aneurysms and acute aortic syndromes, Nat. Rev. Cardiol. 18 (5) (2021) 331–348, https://doi.org/10.1038/s41569-020-00472-6.
- [2] C. DeCarlo, C.A. Latz, L.T. Boitano, Y. Kim, A. tanious, S.I. Schwartz, R. Patell, J. Mohebali, A. Dua, Prognostication of asymptomatic penetrating aortic ulcers: a modern approach, Circulation 144 (14) (2021) 1091–1101, https://doi.org/ 10.1161/circulationaba.121.054710.
- [3] T. D'Annoville, B.A. Ozdemir, P. Alric, C.H. Marty-Ané, L. Canaud, Thoracic endovascular aortic repair for penetrating aortic ulcer: literature review, Ann. Thorac. Surg. 101 (6) (2016) 2272–2278, https://doi.org/10.1016/j. athoracsur.2015.12.036.
- [4] E.C. Colacchio, F. Squizzato, M. Piazza, M. Menegolo, F. Grego, M. Antonello, Clinical and imaging predictors of disease progression in type B aortic intramural hematomas and penetrating aortic ulcers: a systematic review, Diagnostics 12 (11) (2022) 2727. https://doi.org/10.3390/diagnostics12112727.
- [5] J. Li, J. Huang, J. Zhao, Y. Tang, The characteristic and treatment of penetrating aortic ulcer in acute symptomatic patients, Chin. J. Vasc. Surg. 2 (1) (2017) 50–53, https://doi.org/10.3760/cma.i.issn.2096-1863.2017.01.012.
- [6] S. Salim, M. Machin, B.O. Patterson, C. Bicknell, The management of penetrating aortic ulcer, Hearts 1 (1) (2022) 5–13, https://doi.org/10.3390/hearts1010003.
- [7] S. Wolk, L.S. Prange, M. Kapalla, F. Schaal, N. Weiss, R.T. Hoffmann, C. Reeps, Midterm survival after aortic repair versus conservative treatment in patients with penetrating aortic ulcer, Vasa 53 (4) (2024) 255–262, https://doi.org/10.1024/ 0301-1526/a001128.
- [8] H. Meng, V.M. Tutino, J. Xiang, A. Siddiqui, High WSS or low WSS? Complex interactions of hemodynamics with intracranial aneurysm initiation, growth, and rupture: toward a unifying hypothesis, AJNR Am. J. Neuroradiol. 35 (7) (2014) 1254–1262.

- [9] Y. Fang, D. Wu, K.G. Birukov, Mechanosensing and mechanoregulation of endothelial cell functions, Compr. Physiol. 9 (2) (2019) 873–904, https://doi.org/ 10.1002/cphy.c180020
- [10] I.A. Tamargo, K.I. Baek, Y. Kim, C. Park, H. Jo, Flow-induced reprogramming of endothelial cells in atherosclerosis, Nat. Rev. Cardiol. 20 (11) (2023) 738–753, https://doi.org/10.1038/s41569-023-00883-1.
- [11] J.J. Wentzel, Y.S. Chatzizisis, F.J.H. Gijsen, G.D. Giannoglou, C.L. Feldman, P. H. Stone, Endothelial shear stress in the evolution of coronary atherosclerotic plaque and vascular remodelling: current understanding and remaining questions, Cardiovasc. Res. 96 (2) (2012) 234–243, https://doi.org/10.1093/cvr/cvs217.
- [12] K. Urschel, M. Tauchi, S. Achenbach, B. Dietel, Investigation of wall shear stress in cardiovascular research and in clinical practice-from bench to bedside, Int. J. Mol. Sci. 22 (11) (2021) 5635, https://doi.org/10.3390/ijms22115635.
- [13] H.T. Sun, K.Y. Sze, A.Y.S. Tang, A.C.O. Tsang, A.C.H. Yu, K.W. Chow, Effects of aspect ratio, wall thickness and hypertension in the patient-specific computational modeling of cerebral aneurysms using fluid-structure interaction analysis, Eng. Appl. Comp. Fluid 13 (2019) 229–244, https://doi.org/10.1080/ 19942060.2019.1572540.
- [14] O. Mutlu, H.E. Salman, H. Al-Thani, A. El-Menyar, U.A. Qidwai, H.C. Yalcin, How does hemodynamics affect rupture tissue mechanics in abdominal aortic aneurysm: focus on wall shear stress derived parameters, time-averaged wall shear stress, oscillatory shear index, endothelial cell activation potential, and relative residence time, Comput. Biol. Med. 154 (2023), https://doi.org/10.1016/j.compbiomed.2023.106609.
- [15] A. Rizza, V. Castiglione, K. Capellini, C. Palmieri, E. Gasparotti, S. Berti, S. Celi, Role of numerical simulations in the management of acute aortic syndromes, Front. Cardiovasc. Med. 11 (2024), https://doi.org/10.3389/fcvm.2024.1309840.
- [16] C. Stokes, D. Ahmed, N. Lind, F. Haupt, D. Becker, J. Hamilton, V. Muthurangu, H. Tengg-Kobligk, G. Papadakis, S. Balabani, V. Díaz-Zuccarini, Aneurysmal growth in type-B aortic dissection: assessing the impact of patient-specific inlet conditions on key haemodynamic indices, J. R. Soc. Interface 20 (206) (2023), https://doi.org/10.1098/rsif.2023.0281.
- [17] N.T. Philip, S. Bolem, B.J. Sudhir, B.S.V. Patnaik, Hemodynamics and biomechanics of morphologically distinct saccular intracranial aneurysms at bifurcations: idealised vs Patient-specific geometries, Comput. Methods Programs Biomed. 227 (2022) 107237, https://doi.org/10.1016/j.cmpb.2022.107237.
- [18] A.A. Valencia, F. Torres, Effects of hypertension and pressure gradient in a human cerebral aneurysm using fluid structure interaction simulations, J. Mech. Med. Biol. 17 (1) (2017). https://doi.org/10.1142/S021951941750018X.
- [19] C. Valeti, S. Bolem, A.K. Alagan, B.J. Sudhir, S.K. Kannath, B. Akhade, G. Matham, K. Krishnakumar, B.S.V. Patnaik, Influence of wall thickness on the rupture risk of a patient-specific cerebral aneurysm: a fluid-structure interaction study, Phys. Fluids 36 (2024) 091904, https://doi.org/10.1063/5.0219980.
- [20] J.M. Zhan, T.D. Lu, Z.Y. Yang, W.Q. Hu, W. Su, Influence of the flow field and vortex structure of patient-specific abdominal aortic aneurysm with intraluminal thrombus on the arterial wall, Eng. Appl. Comp. Fluid 16 (2022) 2100–2122, https://doi.org/10.1080/19942060.2022.2131628.
- [21] K. Bäumler, V. Vedula, A.M. Sailer, J. Seo, P. Chiu, G. Mistelbauer, F.P. Chan, M. P. Fischbein, A.L. Marsden, D. Fleischmann, Fluid-structure interaction simulations of patient-specific aortic dissection, Biomech. Model. Mechanobiol. 19 (5) (2020) 1607–1628, https://doi.org/10.1007/s10237-020-01294-8.
- [22] X. Wang, M.H. Ghayesh, A. Kotousov, A.C. Zander, J.A. Dawson, P.J. Psaltis, Fluid-structure interaction study for biomechanics and risk factors in Stanford type A aortic dissection, Int. J. Numer. Method Biomed. Eng. 39 (2023) e3736, https://doi.org/10.1002/cnm.3736.
- [23] Z. Jia, J. Mei, W. Ding, X. Zhao, W. Gong, H. Yu, L. Qin, Z. Piao, W. Chen, L. Tang, The pathogenesis of superior mesenteric artery dissection: an in-depth study based on fluid-structure interaction and histology analysis, Comput. Methods Programs Biomed. 226 (2022) 107187, https://doi.org/10.1016/j.cmpb.2022.107187.
- [24] K. Baumler, M. Rolf-Pissarczyk, R. Schussnig, T.P. Fries, G. Mistelbauer, M. R. Pfaller, A.L. Marsden, D. Fleischmann, G.A. Holzapfel, Assessment of aortic dissection remodeling with patient-specific fluid-structure interaction models, IEEE Trans. Biomed. Eng. (2024) 1–17, https://doi.org/10.1109/TBME.2024.3480362.
- [25] F. Auricchio, M. Conti, R.M. Romarowski, Usefulness of computational fluid dynamics in penetrating aortic ulcer, Ann. Cardiothorac. Surg. 8 (4) (2019) 492–493, https://doi.org/10.21037/acs.2019.06.08.
- [26] G. D'Ancona, A. Amaducci, A. Rinaudo, S. Pasta, F. Follis, M. Pilato, R. Baglini, Haemodynamic predictors of a penetrating atherosclerotic ulcer rupture using fluid-structure interaction analysis, Interact. Cardiovasc. Thorac. Surg. 17 (3) (2013) 576–578, https://doi.org/10.1093/icvts/ivt245.
- [27] H. Mansouri, M. Kemerli, R. MacIver, O. Amili, Development of idealized human aortic models for in vitro and in silico hemodynamic studies, Front. Cardiovasc. Med. 11 (2024), https://doi.org/10.3389/fcvm.2024.1358601.
- [28] K.K.L. Wong, D. Wang, J.K.L. Ko, J. Mazumdar, T.T. Le, D. Ghista, Computational medical imaging and hemodynamics framework for functional analysis and assessment of cardiovascular structures, Biomed. Eng. Online 16 (35) (2017), https://doi.org/10.1186/s12938-017-0326-y.
- [29] Y. Zhu, S. Mirsadraee, U. Rosendahl, J. Pepper, X.Y. Xu, Fluid-Structure interaction simulations of repaired type A aortic dissection: a comprehensive comparison with rigid wall models, Front. Physiol. 13 (2022), https://doi.org/10.3389/ fphys.2022.913457.
- [30] C.H. Armour, B. Guo, S. Saitta, S. Pirola, Y. Liu, Z. Dong, X.Y. Xu, Evaluation and verification of patient-specific modelling of type B aortic dissection, Comput. Biol. Med. 140 (2022) 105053, https://doi.org/10.1016/j.compbiomed.2021.105053.

- [31] C.A. Kousera, N.B. Wood, W.A. Seed, R. Torii, D. O'Regan, X.Y. Xu, A numerical study of aortic flow stability and comparison with in vivo flow measurements, J. Biomech. Eng. 135 (1) (2012) 011003, https://doi.org/10.1115/1.4023132.
- [32] R. Schussnig, M. Rolf-Pissarczyk, K. Bäumler, T. Fries, G.A. Holzapfel, M. Kronbichler, On the role of tissue mechanics in fluid–structure interaction simulations of patient-specific aortic dissection, Int. J. Numer. Methods Eng. 125 (14) (2024) e7478, https://doi.org/10.1002/nme.7478.
- [33] X. Wang, X. Li, Computational simulation of aortic aneurysm using FSI method: influence of blood viscosity on aneurismal dynamic behaviors, Comput. Biol. Med. 41 (9) (2011) 812–821, https://doi.org/10.1016/j.compbiomed.2011.06.017.
- [34] A. Karimi, M. Navidbakhsh, A. Shojaei, S. Faghihi, Measurement of the uniaxial mechanical properties of healthy and atherosclerotic human coronary arteries, Mater. Sci. Eng. C Mater. Biol. Appl. 33 (5) (2013) 2550–2554, https://doi.org/ 10.1016/j.msec.2013.02.016.
- [35] S. Badia, F. Nobile, C. Vergara, Robin–Robin preconditioned Krylov methods for fluid–structure interaction problems, Comput. Methods Appl. Mech. Eng. 198 (2009) 2768–2784, https://doi.org/10.1016/j.cma.2009.04.004.
- [36] C.C. Mei, J. Zhang, H.X. Jing, Fluid mechanics of Windkessel effect, Med. Biol. Eng. Comput. 56 (8) (2018) 1357–1366, https://doi.org/10.1007/s11517-017-1775-y.
- [37] S. Aslan, P. Mass, Y.H. Loke, L. Warburton, X. Liu, N. Hibino, L. Olivieri, A. Krieger, Non-invasive prediction of peak systolic pressure drop across coarctation of aorta using computational fluid dynamics, Annu. Int. Conf. IEEE Eng. Med. Biol. Soc. 2020 (2020) 2295–2298, https://doi.org/10.1109/embc44109.2020.9176461.
- [38] A.G. Brown, Y. Shi, A. Marzo, C. Staicu, I. Valverde, P. Beerbaum, P.V. Lawford, D. R. Hose, Accuracy vs. computational time: translating aortic simulations to the clinic, J. Biomech. 45 (3) (2012) 516–523, https://doi.org/10.1016/j.jbiomech.2011.11.041.

- [39] Y. Iida, A. Yoshitake, H. Shimizu, Blood flow into ulcer-like projection of a type B aortic dissection visualized with computational fluid dynamics, J. Thorac. Cardiovasc. Surg. 154 (4) (2017) 1217–1218, https://doi.org/10.1016/j.iteus.2017.04.040
- [40] G.S. Oderich, J.M. Kärkkäinen, N.R. Reed, E.R. Tenorio, G.A. Sandri, Penetrating aortic ulcer and intramural hematoma, Cardiovasc. Intervent. Radiol. 42 (3) (2019) 321–334, https://doi.org/10.1007/s00270-018-2114-x.
- [41] D.P. Nathan, W. Boonn, E. Lai, G.J. Wang, N. Desai, E.Y. Woo, R.M. Fairman, B. M. Jackson, Presentation, complications, and natural history of penetrating atherosclerotic ulcer disease, J. Vasc. Surg. 55 (1) (2012) 10–15, https://doi.org/10.1016/j.jvs.2011.08.005.
- [42] M. Zhou, Y. Yu, R. Chen, X. Liu, Y. Hu, Z. Ma, L. Gao, W. Jian, L. Wang, Wall shear stress and its role in atherosclerosis, Front. Cardiovasc. Med. 10 (2023), https://doi.org/10.3389/fcvm.2023.1083547.
- [43] Y. Higuchi, A. Hirayama, Y. Hamanaka, T. Kobayashi, Y. Sotomi, S. Komatsu, C. Yutani, K. Kodama, Significant contribution of aortogenic mechanism in ischemic stroke: observation of aortic plaque rupture by angioscopy, JACC Asia 2 (6) (2022) 750–759, https://doi.org/10.1016/j.jacasi.2022.07.009.
- [44] J.Z. Li, K.A. Eagle, P. Vaishnava, Hypertensive and acute aortic syndromes, Cardiol. Clin. 31 (4) (2013) 493–501, https://doi.org/10.1016/j.ccl.2013.07.011.
- [45] M.T. Cooney, E. Vartiainen, T. Laatikainen, A. Juolevi, A. Dudina, I.M. Graham, Elevated resting heart rate is an independent risk factor for cardiovascular disease in healthy men and women, Am. Heart J. 159 (4) (2010) 612–619, https://doi.org/ 10.1016/j.ahj.2009.12.029.
- [46] P.M. Khan, S.D. Sharma, S. Chakraborty, S. Roy, Effect of heart rate on the hemodynamics in healthy and stenosed carotid arteries, Phys. Fluids 35 (6) (2023) 061906, https://doi.org/10.1063/5.0153323.